Dalton Transactions

ROYAL SOCIETY OF CHEMISTRY

PAPER

View Article Online
View Journal | View Issue



Cite this: *Dalton Trans.*, 2021, **50**, 14864

# NIR emission of lanthanides for ultrasensitive luminescence manometry—$Er^{3+}$-activated optical sensor of high pressure†

Marcin Runowski, *[a] Teng Zheng, [a] Przemysław Woźny [a] and Peng Du *[b]

Received 11th August 2021,
Accepted 10th September 2021

DOI: 10.1039/d1dt02681j

rsc.li/dalton

Pressure is an important physical parameter and hence its monitoring is very important for different industrial and scientific applications. Although commonly used luminescent pressure sensors (ruby—$Al_2O_3$:$Cr^{3+}$ and $SrB_4O_7$:$Sm^{2+}$) allow optical monitoring of pressure in compressed systems (usually in a diamond anvil cell; DAC), their detection resolution is limited by sensitivity, *i.e.*, pressure response in a form of the detected spectral shift. Here we report, a breakthrough in optical pressure sensing by developing an ultrasensitive NIR pressure sensor ($d\lambda/dP$ = 1.766 nm $GPa^{-1}$). This luminescent manometer is based on the optically active $YVO_4$:$Yb^{3+}$–$Er^{3+}$ phosphor material which exhibits the largest spectral shift as a function of pressure compared to other luminescent pressure gauges reported elsewhere. In addition, thanks to the locations of excitation and emission in the NIR range, the developed optical manometer allows high-pressure measurements (without spectral overlapping/interferences) of various luminescent organic and inorganic materials, which are typically excited and can emit in the UV-vis spectral ranges.



## 1. Introduction

High-pressure compression of materials can lead to various interesting alterations of their physicochemical properties, including shrinking of unit cell volume (shortening of bond lengths), structural symmetry variations, defect formation, the emergence of new structures/phases, formation of novel materials, *etc.*[1–5] The development of noninvasive precise and accurate optical manometers has been stimulated by the challenging requirements of higher sensitivity, arising from the scientific research studies in diverse pressure regimes, from vacuum to high-pressure regions (over 100 GPa).[6,7] The spectroscopic properties of materials under high-pressure conditions can be monitored by performing experiments in a diamond anvil cell (DAC) based on the assembly setup of a metal housing, two highly transparent diamond anvils, pressure transmitting medium (PTM), metal gasket and screws to squeeze and compress the material studied.[8] For determination of the hydrostatic pressure in a DAC chamber, inorganic materials doped with lanthanide and d-block metal ions are usually used as optical manometers.[6,7,9] Currently, at very high pressure (above 10–20 GPa), the sensitivities of the commonly used ruby ($Al_2O_3$:$Cr^{3+}$; $d\lambda/dP \approx 0.35$ nm $GPa^{-1}$)[8,10] and $SrB_4O_7$:$Sm^{2+}$ ($d\lambda/dP \approx 0.25$ nm $GPa^{-1}$) pressure sensors[11,12] may be fairly enough due to the hydrostatic limits of the commonly used PTM, leading to the occurrence of some pressure gradient in the chamber of DAC. However, in the relatively low pressure range (up to few GPa), where numerous phase transitions of soft, organic materials may occur, new manometers with higher sensitivity (large spectral shift) are continuously pursued in order to realize accurate pressure determination (resolve the similar pressure values in the investigated system) for phase transition detection, monitoring physical and chemical behaviour under high-pressure conditions, and so forth.

Lanthanide ($Ln^{3+/2+}$) doped inorganic compounds are versatile functional materials, which are applied in diverse fields, such as bio-imaging, anti-counterfeiting, pressure and temperature sensing, modern lighting techniques, microscopy, *etc.*[13–16] This is due to the specific spectroscopic features that originated from their ladder-like electronic structure, including multi-range absorption/emission (UV-vis-NIR); absence of autofluorescence; the forbidden (by Laporte selection rules) character of the intrinsic 4f–4f transitions, leading to long emission lifetimes;[17] shielding of the 4f electrons by 5s and 5p ones, resulting in sharp emission/absorption lines; crystal-

[a]*Adam Mickiewicz University, Faculty of Chemistry, Uniwersytetu Poznańskiego 8, 61-614 Poznań, Poland. E-mail: runowski@amu.edu.pl*
[b]*Department of Microelectronic Science and Engineering, School of Physical Science and Technology, Ningbo University, 315211 Ningbo, Zhejiang, China. E-mail: dupeng@nbu.edu.cn*

†Electronic supplementary information (ESI) available: Fitting parameters; determined spectral positions of Stark sublevels for $Er^{3+}$ $^4I_{13/2} \rightarrow {}^4I_{15/2}$ transition; energies of the peak centroids; luminescence decay curve; non-normalized spectra as a function of pressure and temperature. See DOI: 10.1039/d1dt02681j

field effects, *etc.*[18,19] The Stokes (down-shifting) and anti-Stokes type (up-conversion) emissions can be triggered by the use of different excitation light sources, from UV to NIR, depending on the host matrix type and the incorporated $Ln^{3+/2+}$ ions.[8,20,21] In the case of optical pressure sensing, the NIR excitation/emission may be very beneficial because it can eliminate some interference factors, namely fluorescence of diamonds and PTM; autofluorescence of particular organic/inorganic compounds studied; and most importantly intense emission of $Cr^{3+}$ and $Sm^{2+}$ in the visible range, which may sometimes overlap with the luminescence of optically active samples, thus hampering spectroscopic measurements under pressure.[22] In fact, some recent reports showed good pressure sensitivity of NIR optical manometers, such as $Er^{3+}$-doped $YPO_4$ ($d\lambda/dP \approx 0.539$ nm $GPa^{-1}$)[23] and $NaBiF_4$ ($d\lambda/dP \approx -0.8$ nm $GPa^{-1}$)[24] materials. In general, the pressure-induced variations of the electronic structure of $Ln^{3+/2+}$ ions in compressed materials allow the determination of different spectroscopic parameters, such as the spectral shift of the emission bands, changes in intensity ratios, bandwidth, shortening of luminescence lifetimes, *etc.*, which can be further utilized for optical manometry.

Up to now, to the best of our knowledge, the most sensitive optical manometer reported was $BaLi_2Al_2SiN_6$:0.01$Eu^{2+}$, which shows very good pressure sensitivity, *i.e.*, $d\lambda/dP = 1.58$ nm $GPa^{-1}$.[25] In this work, we report an ultra-sensitive pressure sensor based on the $YVO_4$:$Yb^{3+}$–$Er^{3+}$ luminescent material, operating in the NIR region (≈1500–1600 nm), based on the Stark components of the $^4I_{13/2} \rightarrow {}^4I_{15/2}$ transition of $Er^{3+}$, exhibiting pressure-induced spectral shift $d\lambda/dP = 1.766$ nm $GPa^{-1}$—a new record in pressure sensitivity. The developed optical manometer is especially beneficial for resolving similar pressure values under mild-pressure conditions (up to a few GPa), where the phase transitions of most organic compounds take place. Moreover, due to the possibility of NIR laser excitation and the location of the emission signal in the NIR region, using the developed sensor, one can avoid potential interferences of background autofluorescence of some organic species and inorganic compounds studied to effectively realize phase transition detection and physicochemical characterization under high-pressure conditions.

## 2. Results and discussion

### 2.1. Characteristics of the sensor material

The luminescent pressure sensor is based on inorganic, submicron-sized particles of $YVO_4$ co-doped with 20 mol% of $Yb^{3+}$ and 2 mol% of $Er^{3+}$ ions. The exact elemental composition of the synthesized compound, determined by the inductively coupled plasma-optical emission spectroscopy (ICP-OES) method is: $Y_{0.748}Yb_{0.228}Er_{0.024}VO_4$. The particles crystallize in the structure of zircon-type tetragonal $YVO_4$, the space group $I4_1/amd$ (bulk modulus, $B_0 = 130(3)$ GPa), where the part of $Y^{3+}$ ions is substituted with $Yb^{3+}$ and $Er^{3+}$ ions, with local point symmetry $D_{4h}$. The material was synthesized using a hydrothermal approach and further calcination (≈1273 K), ensuring its high thermal stability and very good crystallinity of the final particles.[26]

Combining the abovementioned benefits with a relatively low phonon energy of the vanadate crystal lattice (≈900 $cm^{-1}$), the lanthanide-doped $YVO_4$ phosphors (luminophores) are generally considered as good and effective (down-shifting) emitters.[27–32] Moreover, in the case of the investigated material $YVO_4$:$Yb^{3+}$–$Er^{3+}$, due to the high absorption cross-section of $Yb^{3+}$ and good emitting properties of $Er^{3+}$ (with rich energy level structure), this compound is known as a good up-converting emitter upon 975 nm excitation.[33] The synthesis details, structural and morphological characteristics, and upconverting ($\lambda_{ex}$ = 975 nm) luminescence properties (including its upconversion emission as a function of temperature, vacuum and excitation power) are given and discussed in detail in our previous study.[26] Moreover, in our other report, we investigated the upconverting properties of the nano-sized (non-calcined) $YVO_4$:$Yb^{3+}$–$Er^{3+}$ material under high-pressure conditions (up to ≈11 GPa).[34] Importantly, in that report, using high-pressure luminescence spectroscopy, we have observed around 8 GPa phase transitions of the material that were also clearly documented by the others and confirmed with XRD and Raman spectroscopy (phase transition to a tetragonal, scheelite-type structure, space group $I4_1/m$, local point symmetry $C_{4h}$, and $B_0 = 138(8)$ Gpa).[35–37]

### 2.2. High-pressure structural studies—Raman spectroscopy

First, it is worth noting that in this work, we have performed the spectroscopic measurements for the material studied up to ≈6.5 GPa, *i.e.*, below the pressure value of the mentioned phase transition in order to avoid the potential nonmonotonic behavior of the determined spectroscopic parameters and ensure the reversibility of the monitored changes, which are important for pressure sensing applications. In order to confirm the structural stability of the investigated material and investigate the behavior of the phonon energies of the crystal lattice under high-pressure conditions, we have measured the Raman spectrum of the $YVO_4$:$Yb^{3+}$–$Er^{3+}$ material in compression–decompression cycles. The spectra presented in Fig. 1 start from 600 $cm^{-1}$ because in the lower energy region (smaller wavenumber values), the artificial luminescence contributions biased the recorded spectra obscuring the low-intensity and low-energy Raman modes, typically observed for the pure (undoped) $YVO_4$ materials at around 154, 259, 376 and 487 $cm^{-1}$.[37,38] However, from the luminescence point of view, the most important are the recorded high-energy phonon modes that are responsible for the phonon-assisted energy transfer and luminescence quenching processes. In all spectra, three high-energy bands are clearly observed, being initially located at around 819, 840 and 894 $cm^{-1}$. These bands correspond to the Raman active modes $\nu_3(B_g)$, $\nu_3(E_g)$ and $\nu_1(A_g)$, respectively.[37] With increasing pressure, all the mentioned peaks shift toward higher energies (higher wavenumber values) with shift rates of about 5.40, 5.08 and 5.55 $cm^{-1}$ $GPa^{-1}$, respectively, which can be clearly observed in Fig. 1.

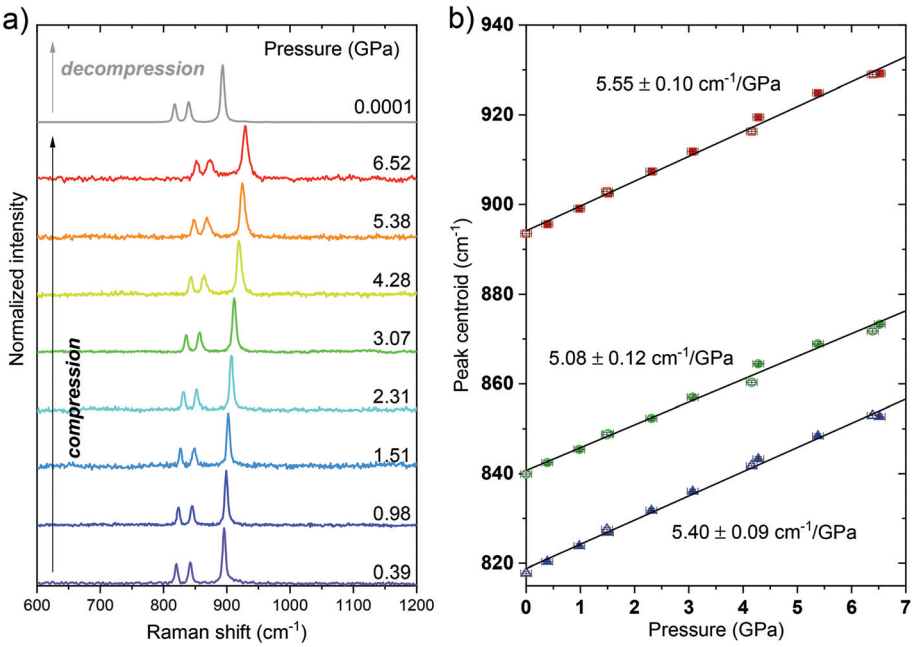


**Fig. 1** (a) Raman spectra and (b) the determined energies of the observed high-energy phonon modes as a function of pressure; the continuous lines represent the applied linear fits; the filled and empty symbols are the data points determined based on the measurements performed during the compression and decompression cycles, respectively.

Importantly, the spectral shifts observed with pressure are fully reversible as the peak centroids determined during the decompression process (the empty symbols in Fig. 1b) are consistent with the data from the compression cycle. The decreasing signal-to-noise ratio and broadening of the peaks with pressure are typical, reversible effects observed in the Raman spectra of the compressed materials, which are related to the decreasing crystallinity level and increasing strains of the crystals, in respect to the material studied at ambient conditions.[39] The obtained results agree with the literature data reported for pure $YVO_4$ materials.[37,38]

### 2.3. High-pressure luminescence studies

Fig. 2a presents the down-shifting emission spectra of the material studied in the NIR range, corresponding to the $^4I_{13/2} \rightarrow {}^4I_{15/2}$ radiative transition of $Er^{3+}$ (centered around 1550 nm), as measured under the high-pressure conditions upon the 975 nm laser excitation. The observed emission is a consequence of the effective excitation of $Yb^{3+}$ ions in resonance to the $^2F_{7/2} \rightarrow {}^2F_{5/2}$ transition, a subsequent resonant energy transfer to the excited level $^4I_{11/2}$ of $Er^{3+}$ and further non-radiative relaxation to the emitting level $^4I_{13/2}$ of $Er^{3+}$ (see the energy level diagram in Fig. 3). It is clearly seen from the spectra that the high-pressure compression of the material induces a spectral shift of the crystal-field components (Stark sub-levels) of the $^4I_{13/2} \rightarrow {}^4I_{15/2}$ transition of $Er^{3+}$ as well as changes the shape of the spectra, *i.e.*, the relative intensities of the components and the level of their overlapping and spectral width. Two main effects are responsible for the observed changes, namely: (I) pressure-enhanced nephelauxetic effect, *i.e.* increased covalency of bonding in the compressed material, resulting in a decreasing energy separation between the ground and excited levels of $Er^{3+}$ that leads to the observed red-shift of the crystal field components on pressure; (II) pressure-enhanced crystal-field strength, due to stronger interactions between $Er^{3+}$ ions and shorter interionic distances ($Er^{3+}$–$O^{2-}$) in the compressed structure, which leads to larger splitting of the observed Stark sub-levels.[8,25,40,41] Due to the fact, that these two effects are superimposed, in general, the low-energy emission lines exhibit larger spectral shifts with pressure compared to the high-energy Stark sub-levels of the transition (see the crystal-field splitting scheme in Fig. 3). In fact, such a situation occurs in our case, as clearly observed in Fig. 2b, demonstrating the spectral positions of the peak centroids for different crystal-field components and the shift rates determined on pressure (by linear fits). The high-energy Stark sub-level located around 1500 nm reveals a significant blue-shift ($d\lambda/dP = -0.740$ nm $GPa^{-1}$), whereas the low-energy peaks located around 1600 nm exhibit large red-shifts ($d\lambda/dP = 1.282$ and 1.766 nm $GPa^{-1}$). The determined shift rates, currently classify the developed sensor as the most sensitive luminescent manometer (see Table 1). The details, *i.e.*, fitting parameters for the analysed seven crystal-field components are given in Table S1 in the ESI data.† Whereas the energies for the determined peak centroids as a function of pressure and the calculated shift rates ($cm^{-1}$ $GPa^{-1}$) are given in Fig. S1.† Please note that we correlated with pressure only those peaks that were present in the whole measured pressure range and did not overlap too much with each other, allowing the determination of their centroids. In addition, based on the recorded

 

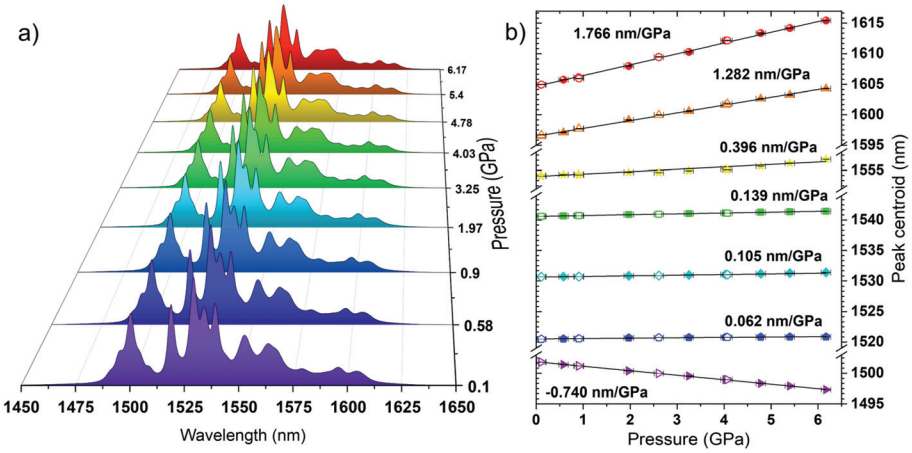


**Fig. 2** (a) The NIR luminescence spectra of the $YVO_4$:$Yb^{3+}$–$Er^{3+}$ sample ($\lambda_{ex}$ = 975 nm), measured as a function of pressure. (b) Determined spectral positions of the seven Stark sub-levels, corresponding to the $^4I_{13/2} \rightarrow {}^4I_{15/2}$ transition of $Er^{3+}$ as a function of pressure; the continuous lines represent the applied linear fits; the filled and empty symbols are the data points determined based on the measurements performed during the compression and decompression cycles, respectively.

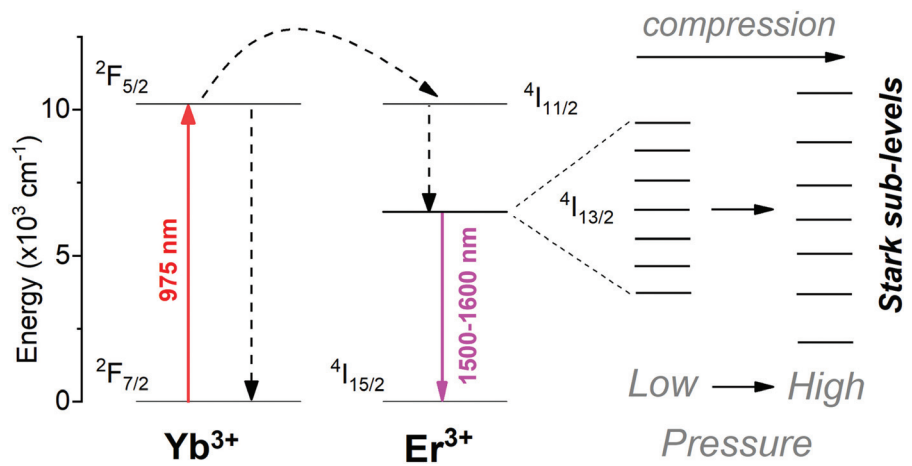


**Fig. 3** Energy level diagram representing the radiative and nonradiative processes occurring in the studied $Yb^{3+}$–$Er^{3+}$ system, emphasizing the crystal field splitting of the $^4I_{13/2}$ level of $Er^{3+}$ at ambient and high-pressure conditions, resulting in the formation of several Stark sub-levels for the $^4I_{13/2} \rightarrow {}^4I_{15/2}$ transition.

luminescence decay curve (at ambient conditions) presented in Fig. S2† ($\lambda_{ex}$ = 975 nm; $\lambda_{em}$ = 1550 nm), we have determined the effective lifetime $\left(\tau_{eff} = \int t \cdot I dt / \int I dt\right)$ for the discussed NIR emission of $Er^{3+}$, *i.e.*, $\tau \approx 1.42$ ms, which defines the temporal response of the sensor.

The non-normalized emission spectra presented in Fig. S3 and S4† (recorded during compression and decompressions runs, respectively) show how the intensity of the bands changes with pressure. It can be observed that around 6 GPa, the intensity of the bands is approximately a half of the intensity of the initial spectrum. Importantly, these changes are reversible as the intensity is almost completely recovered after the decompression process. Here, it is worth noting that, in general, there are three main mechanisms responsible for luminescence quenching of lanthanide ions under high-pressure conditions, namely: (I) pressure-induced plastic deformations, leading to the formation of crystal defects; (II) multi-phonon relaxation enhanced with pressure, due to the increasing phonon energies of the compressed host matrices; and (III) improved cross-relaxation processes, as a result of decreasing interionic distances in the compressed materials.[8,40–42] However, only the first mechanism may have a minor contribution to the signal deterioration with pressure (because after the decompression process, the signal intensity is recovered roughly in 90%, as can be observed in Fig. S4†) and the second and third mechanisms are not expected to occur in the system studied. This is due to the following reasons: (I) the observed intensity changes are almost completely reversible; (II) the considered NIR emission occurs from the lowest excited level, situated around 6500 cm$^{-1}$ above the

Table 1 Comparison of high-pressure sensitivities of different luminescent manometers used for optical pressure sensing

| Host | Emitting ion | Transitions | $\lambda$ (nm) | T-shift (nm $K^{-1}$) | Sensitivity line shift (nm $GPa^{-1}$) | Ref. |
|---|---|---|---|---|---|---|
| $YVO_4$ | $Er^{3+}$ | $^4I_{13/2} \rightarrow {}^4I_{15/2}$ (stark) | 1605 | $-5.16 \times 10^{-3}$ | 1.766 | This work |
| | | $^4I_{13/2} \rightarrow {}^4I_{15/2}$ (stark) | 1596 | $-4.04 \times 10^{-3}$ | 1.282 | |
| | | $^4I_{13/2} \rightarrow {}^4I_{15/2}$ (stark) | 1502 | $3.63 \times 10^{-3}$ | −0.740 | |
| $YPO_4$ | $Er^{3+}$ | $^4I_{13/2} \rightarrow {}^4I_{15/2}$ (stark) | 1589 | $-1.78 \times 10^{-3}$ | 0.539 | 23 |
| $Al_2O_3$ (ruby) | $Cr^{3+}$ | $^2E \rightarrow {}^4A_2$ | 694 | $\approx 7 \times 10^{-3}$ | 0.365 | 10,44 and 48 |
| $YAlO_3$ | $Cr^{3+}$ | $^2E \rightarrow {}^4A_2$ | 723 | $7.6 \times 10^{-3}$ | 0.70 | 48 |
| $YF_3$ | $Er^{3+}$ | $^4F_{9/2} \rightarrow {}^4I_{15/2}$ (stark) | 665 | $-3 \times 10^{-4}$ | 0.1855 | 49 |
| $NaBiF_4$ | $Er^{3+}$ | $^4I_{13/2} \rightarrow {}^4I_{15/2}$ (stark) | 1503 | — | −0.8 | 24 |
| $YAlO_3$ | $Nd^{3+}$ | $^4F_{3/2} \rightarrow {}^4I_{9/2}$ (stark) | 875 | $1 \times 10^{-6}$ | −0.13 | 48 |
| $Gd_3Sc_2Ga_3O_{12}$ | $Nd^{3+}$ | $^4F_{3/2} \rightarrow {}^4I_{9/2}$ (stark) | 935 | — | ~0.632 | 50 |
| $Y_3Al_5O_{12}$ | $Eu^{3+}$ | $^5D_0 \rightarrow {}^7F_1$ | 591 | $-5.4 \times 10^{-4}$ | 0.197 | 51 |
| $EuPO_4$ | $Eu^{3+}$ | $^5D_0 \rightarrow {}^7F_0$ | 580 | — | ~0.27 | 52 |
| $Y_3Al_5O_{12}$ | $Sm^{3+}$ | $^4G_{5/2} \rightarrow {}^6H_{7/2}$ (stark) | 618 | $2.3 \times 10^{-4}$ | 0.30 | 53 |
| SrFCl | $Sm^{2+}$ | $^5D_0 \rightarrow {}^7F_0$ | 690 | $-2.3 \times 10^{-3}$ | 1.11 | 54 |
| $SrB_4O_7$ | $Sm^{2+}$ | $^5D_0 \rightarrow {}^7F_0$ | 685 | $-1 \times 10^{-4}$ | 0.255 | 55 |
| $SrB_2O_4$ | $Sm^{2+}$ | $^5D_0 \rightarrow {}^7F_0$ | 685 | $-1 \times 10^{-4}$ | 0.244 | 56 |
| $BaLi_2Al_2Si_2N_6$ | $Eu^{2+}$ | 5d → 4f | 532 | — | 1.58 | 25 |
| $KMgF_3$ | $Eu^{2+}$ | 5d → 4f | 360 | — | ~0.13 | 57 |
| CeN-PVDF | $Ce^{3+}$ | 5d → 4f | 327 | — | 0.28 | 58 |
| CeS-PVDF | $Ce^{3+}$ | 5d → 4f | 340 | — | 0.1 | 58 |
| $LaPO_4$ | $Tm^{3+}$ | $^1G_4 \rightarrow {}^3H_6$ | 475 | $-2 \times 10^{-3}$ | 0.1 | 59 |
| | | $^3H_4 \rightarrow {}^3H_6/{}^1G_4 \rightarrow {}^3H_6$ | 800/475 | — | 8% (band ratio) | |
| $Y_6Ba_4(SiO_4)_6F_2$ | $Ce^{3+}$ | $^2D_J \rightarrow {}^2F_J$ (5d → 4f) emission | 466 | — | 0.63 | 8 |
| | | | | | 1.5% (FWHM) | |
| | | $^2F_J \rightarrow {}^2D_J$ (4f → 5d) excitation | 342 | — | 2.5% (FWHM) | |
| $SrF_2$ | $Er^{3+}$ | $^4F_{9/2} \rightarrow {}^4I_{15/2}$ | 653 | — | 7.7% (lifetime) | 60 |
| | | $^4S_{3/2} \rightarrow {}^4I_{15/2}$ | 538 | | 6.4% (lifetime) | |
| | | $^2H_{11/2} \rightarrow {}^4I_{15/2}$ | 516 | | 6.2% (lifetime) | |

ground level, and the highest-energy phonon mode has an energy of around 930 $cm^{-1}$ (at ≈6.5 GPa), so for the multiphonon relaxation the required number of phonons is 7 (in general, the maximum number of phonons leading to the effective multiphonon relaxation is considered to be 3–5);[26] and (III) below the energy of the emitting level $^4I_{13/2}$, there are no other lower lying excited states in the system studied (neither in $Yb^{3+}$ nor in $Er^{3+}$ ions), so the cross-relaxation processes should not affect that level. That is why the observed emission is not significantly quenched at pressure (compared to other luminescent materials) and the probable mechanisms responsible for quenching may be related to the decreasing crystallinity and increasing strains in the crystals, as well as the increased energy migration to traps and defect states, leading to the less efficient $Yb^{3+} \rightarrow Er^{3+}$ energy transfer and lower probability of radiative relaxation from the excited state $^4I_{13/2}$ in the compressed material.

### 2.4. Temperature effect on luminescence properties

In developing new luminescent pressure-sensors, one should not neglect the impact of temperature on the spectral position of the emission line used for sensing purposes, *i.e.*, the so-called temperature correction or thermal drift. This is because more and more experiments are performed simultaneously under extreme conditions of both pressure and temperature (the compressed and heated-cooled systems). Hence, the optimal sensor should exhibit a negligible temperature-dependence or only small (compared to the corresponding shift in pressure) and well-defined spectral shifts.[41,43] Fortunately, for the emission lines of the developed sensor, the determined thermal drifts are small and linear, *e.g.*, $d\lambda/dT = -5.16 \times 10^{-3}$, $-4.04 \times 10^{-3}$ and $3.63 \times 10^{-3}$ nm $K^{-1}$, for the most pressure-sensitive Stark sub-levels located initially at ≈1605, 1596 and 1502 nm, respectively (see Fig. 4 and S5†). Importantly, the determined temperature drifts are smaller than that in the commonly used pressure sensor—ruby ($d\lambda/dT = 7 \times 10^{-3}$ nm $K^{-1}$)[44] and they are similar to those of other reported luminescent pressure sensors (see Table 1). In addition, the energies for the determined peak centroids as a function of temperature and the calculated shift rates ($cm^{-1}$ $K^{-1}$) are given in Fig. S6.†

Besides, the often underestimated thermal effect is signal deterioration at elevated temperatures, which may affect the precision and accuracy of pressure sensing under extreme conditions of both factors. The main mechanism responsible for luminescence quenching of lanthanide ions at elevated temperatures is multiphonon relaxation as the phonon energy increases with temperature as well.[45–47] However, in the case of the developed sensor material, the required number of phonons is too high to allow effective multiphonon relaxation (as was described in the previous paragraph concerning signal intensity changes with pressure), that is why the mentioned quenching mechanism should have a negligible contribution. The analysis of signal intensity as a function of temperature confirms this assumption, as the absolute luminescence intensity almost does not change with temperature, as can be observed in the emission spectra presented in Fig. S5.†

 

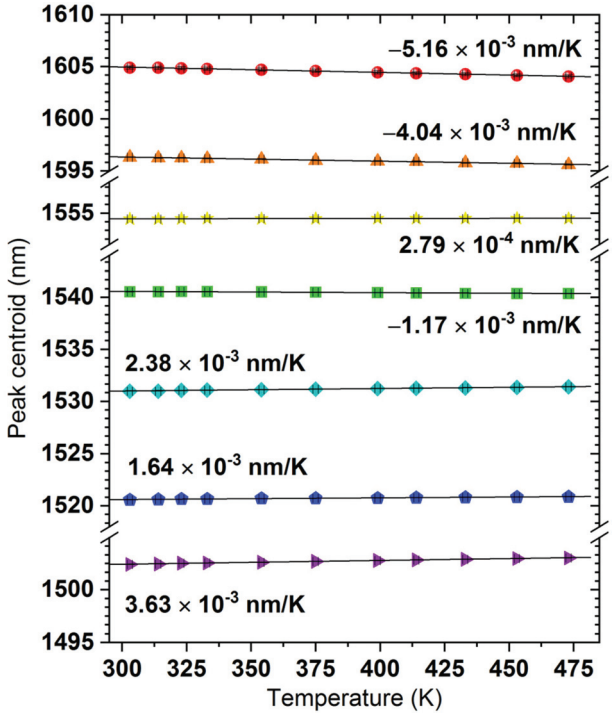


Fig. 4 Determined spectral positions, *i.e.*, peak centroids of the Stark sub-levels (initially located at ≈1502, 1521, 1531, 1541, 1554, 1596 and 1605 nm) as a function of temperature, corresponding to the $^4I_{13/2} \rightarrow {}^4I_{15/2}$ transition of $Er^{3+}$ in the $YVO_4$:$Yb^{3+}$–$Er^{3+}$ material ($\lambda_{ex}$ = 975 nm).

## 3. Conclusions

In this work, we presented a development of the ultrasensitive ($d\lambda/dP$ = 1.766 nm $GPa^{-1}$), optical pressure sensor (current leader in sensitivity) based on the luminescent lanthanide-doped material $YVO_4$:$Yb^{3+}$–$Er^{3+}$, which is five times more sensitive than the commonly used ruby-based sensors. High-sensitivity of the sensor was achieved by monitoring its NIR emission, namely the crystal-field components (Stark sub-levels) of the $^4I_{13/2} \rightarrow {}^4I_{15/2}$ transition of $Er^{3+}$, centred around 1550 nm. Another benefit of this luminescent manometer is the possibility of excitation in the NIR range (thanks to energy transfer $Yb^{3+} \rightarrow Er^{3+}$), utilizing commercially available and low-cost diode lasers, emitting at around 975/980 nm. It is worth noting that the applied low-energy NIR light does not damage and easily penetrates many materials/media. Moreover, in contrast to blue-green lasers (used for ruby and $Sm^{2+}$ excitation), NIR light does not produce background autofluorescence, because, in general, most of the organic species and inorganic compounds do not produce luminescence upon excitation in the NIR spectral range. Importantly, thanks to the high sensitivity of the developed sensor material, it allows very accurate pressure sensing (depending on the resolution of the detection system, pressure range studied and the pressure transmitting medium used). The developed sensor might be especially useful for the relatively low-pressure sensing (up to a few GPa), especially in the case of the experiments performed with soft, organic materials, where multiple phase transitions may occur in a narrow pressure range. In such a case, a very sensitive material (*e.g.* showing large spectral shift) is required to resolve the similar pressure values of the studied system, allowing the detection of phase transitions and monitoring the changes of various physical and chemical parameters during the compression–decompression cycles.

## 4. Experimental section

As was already mentioned, the detailed synthesis protocol of the material studied can be found in our previous article.[26] Raman spectra were recorded in backscattering geometry by using a Renishaw InVia confocal micro-Raman system, using a grating with 1800 grooves per mm (spectral resolution better than 1 $cm^{-1}$) and a power-controlled 785 nm laser diode. The laser beam was focused by using an Olympus ×20 SLMPlan N long working distance objective. Emission spectra in the NIR range were recorded by using an Andor Shamrock 500 spectrometer equipped with an InGaAs CCD camera (Andor). The excitation light source was a tunable CW Ti:sapphire laser (Spectra Physics 3900-S) adjusted at 975 nm and pumped with a 15 W 532 nm laser (Spectra Physics Millenia). Emission decay curve was recorded using a 200 MHz LeCroy WS424 oscilloscope coupled with a photomultiplier tube (PMT)—Hamamatsu H10330C-75—and a tunable EKSPLA/NT342/3/UVE 10 ns pulsed laser, *i.e.*, optical parametric oscillator (OPO), operating at 10 Hz repetition rate. Luminescence measurements under high-pressure conditions were performed in a diamond anvil cell (DAC), using a back illuminated configuration with 180° detection geometry. The laser beam was focused on the sample placed in a gasket hole and the emission signal was collected from the opposite side of the DAC.

The DAC device was made at Universität Paderborn, in Germany. The culete size (diameter) of the diamond anvils was 400 μm. The pressure inside the DAC chamber was adjusted with four metal screws. The metal gasket used for DAC was made of a stainless-steel sheet, with a thickness of 200 μm, which was pre-indented down to ≈70 μm (sample thickness) and then a hole of size ≈100 μm was made with an electro-driller device. The sample and a single micron-sized ruby ball (<10 μm in diameter) were loaded in the DAC chamber. Subsequently, the pressure transmitting medium (solvent system of methanol/ethanol/water = 16 : 3 : 1(vol.)) was then filled in the DAC chamber to maintain hydrostatic conditions during the compression process. The pressure values were determined with a ruby $R_1$ fluorescence line shift, using 532 nm laser excitation and standard ruby calibration curve available at http://kantor.50webs.com/ruby.htm.

## Conflicts of interest

The authors declare no competing financial interest.

## Acknowledgements

This work was supported by the Polish National Science Centre, grant no. 2016/23/D/ST4/00296 and 2018/31/N/ST5/00636, and by the grant no. POWR.03.02.00-00-I023/17 and POWR.03.02.00-00-i020/17 co-financed by the European Union through the European Social Fund under the Operational Program Knowledge Education Development.



## References

1 J. Sun, Q. Li, H. Zhu, Z. Liu, K. Lin, N. Wang, Q. Zhang, L. Gu, J. Deng, J. Chen and X. Xing, *Adv. Mater.*, 2020, **32**, 1–6.
2 F. Bai, K. Bian, X. Huang, Z. Wang and H. Fan, *Chem. Rev.*, 2019, **119**, 7673–7717.
3 L. Zhang, C. Liu, L. Wang, C. Liu, K. Wang and B. Zou, *Angew. Chem., Int. Ed.*, 2018, **57**, 11213–11217.
4 S. Liu, S. Sun, C. K. Gan, A. G. Del Águila, Y. Fang, J. Xing, T. Thu Ha Do, T. J. White, H. Li, W. Huang and Q. Xiong, *Sci. Adv.*, 2019, **5**, 1–11.
5 Y. N. Zhuravlev and V. V. Atuchin, *Sensors*, 2021, **21**, 3644.
6 S. M. Peak and A. N. Watkins, *ACS Appl. Nano Mater.*, 2020, **3**, 9813–9821.
7 G. Pacchioni, *Nat. Rev. Mater.*, 2021, **6**, 108.
8 M. Runowski, P. Woźny, N. Stopikowska, Q. Guo and S. Lis, *ACS Appl. Mater. Interfaces*, 2019, **11**, 4131–4138.
9 J. W. Gregory, K. Asai, M. Kameda, T. Liu and J. P. Sullivan, *Proc. Inst. Mech. Eng., Part G*, 2008, **222**, 249–290.
10 H. K. Mao, J. Xu and P. M. Bell, *J. Geophys. Res.*, 1986, **91**, 4673–4676.
11 C. Zhao, H. Li, Y. Wang, J. Jiang and Y. He, *High Press. Res.*, 2017, **37**, 18–27.
12 Q. Jing, Q. Wu, L. Liu, J. Xu, Y. Bi, Y. Liu, H. Chen, S. Liu, Y. Zhang, L. Xiong, Y. Li and J. Liu, *J. Appl. Phys.*, 2013, **113**, 023507.
13 C. D. S. Brites, A. Millán and L. D. Carlos, in *Handbook on the Physics and Chemistry of Rare Earths*, 2016, vol. 49, pp. 339–427.
14 R. Marin, D. Jaque and A. Benayas, *Nanoscale Horiz.*, 2021, **6**, 209–230.
15 H. Tang, M. F. Zhang, S. J. Zhang, Y. J. Feng, F. Li and T. R. Shrout, *J. Eur. Ceram. Soc.*, 2013, **33**, 2491–2497.
16 Z. Xia, Y. Zhang, M. S. Molokeev and V. V. Atuchin, *J. Phys. Chem. C*, 2013, **117**, 20847–20854.
17 K. Binnemans, *Chem. Rev.*, 2009, **109**, 4283–4374.
18 F. Auzel, *Chem. Rev.*, 2004, **104**, 139–173.
19 M. D. Dramićanin, *Methods Appl. Fluoresc.*, 2016, **4**, 042001.
20 C. S. Lim, A. S. Aleksandrovsky, M. S. Molokeev, A. S. Oreshonkov, D. A. Ikonnikov and V. V. Atuchin, *Dalton Trans.*, 2016, **45**, 15541–15551.
21 Y. G. Denisenko, V. V. Atuchin, M. S. Molokeev, N. Wang, X. Jiang, A. S. Aleksandrovsky, A. S. Krylov, A. S. Oreshonkov, A. E. Sedykh, S. S. Volkova, Z. Lin, O. V. Andreev and K. Müller-Buschbaum, *J. Mater. Sci. Technol.*, 2021, **76**, 111–121.
22 R. Reisfeld and C. K. Jørgensen, *Lasers and Excited States of Rare Earths*, Springer Berlin Heidelberg, Berlin, 1977, vol. 1, DOI: 10.1007/978-3-642-66696-4.
23 M. Runowski, P. Woźny and I. R. Martín, *J. Mater. Chem. C*, 2021, **9**, 4643–4651.
24 M. A. Antoniak, S. J. Zelewski, R. Oliva, A. Żak, R. Kudrawiec and M. Nyk, *ACS Appl. Nano Mater.*, 2020, **3**, 4209–4217.
25 Y. Wang, T. Seto, K. Ishigaki, Y. Uwatoko, G. Xiao, B. Zou, G. Li, Z. Tang, Z. Li and Y. Wang, *Adv. Funct. Mater.*, 2020, **30**, 2001384.
26 M. Runowski, P. Woźny, S. Lis, V. Lavín and I. R. Martín, *Adv. Mater. Technol.*, 2020, **5**, 1901091.
27 I. E. Kolesnikov, A. A. Kalinichev, M. A. Kurochkin, E. V. Golyeva, A. S. Terentyeva, E. Y. Kolesnikov and E. Lähderanta, *Sci. Rep.*, 2019, **9**, 2043.
28 I. E. Kolesnikov, E. V. Golyeva, A. A. Kalinichev, M. A. Kurochkin, E. Lähderanta and M. D. Mikhailov, *Sens. Actuators, B*, 2017, **243**, 338–345.
29 G. Chen, N. A. Stump, R. G. Haire, J. R. Peterson and M. M. Abraham, *J. Phys. Chem. Solids*, 1992, **53**, 1253–1257.
30 G. Jia, Y. Song, M. Yang, Y. Huang, L. Zhang and H. You, *Opt. Mater.*, 2009, **31**, 1032–1037.
31 Y. Zuo, W. Ling and Y. Wang, *J. Lumin.*, 2012, **132**, 61–63.
32 R. J. Wiglusz, A. Bednarkiewicz and W. Strek, *Inorg. Chem.*, 2012, **51**, 1180–1186.
33 M. Kumar Mahata, T. Koppe, K. Kumar, H. Hofsäss and U. Vetter, *Sci. Rep.*, 2016, **6**, 36342–36352.
34 P. Woźny, M. Runowski and S. Lis, *J. Lumin.*, 2019, **209**, 321–327.
35 J. Ruiz-Fuertes, O. Gomis, S. F. León-Luis, N. Schrodt, F. J. Manjón, S. Ray, D. Santamaría-Pérez, J. A. Sans, H. M. Ortiz, D. Errandonea, C. Ferrer-Roca, A. Segura, D. Martínez-García, V. Lavín, U. R. Rodríguez-Mendoza and A. Muñoz, *Nanotechnology*, 2016, **27**, 025701.
36 X. Wang, I. Loa, K. Syassen, M. Hanfland and B. Ferrand, *Phys. Rev. B: Condens. Matter Mater. Phys.*, 2004, **70**, 064109.
37 F. J. Manjón, P. Rodríguez-Hernández, A. Muñoz, A. H. Romero, D. Errandonea and K. Syassen, *Phys. Rev. B: Condens. Matter Mater. Phys.*, 2010, **81**, 075202.
38 A. Jayaraman, G. A. Kourouklis, G. P. Espinosa, A. S. Cooper and L. G. Van Uitert, *J. Phys. Chem. Solids*, 1987, **48**, 755–759.
39 M. Runowski, A. Bartkowiak, M. Majewska, I. R. Martín and S. Lis, *J. Lumin.*, 2018, **201**, 104–109.
40 K. L. Bray, M. Glasbeek, H. Kunkely and A. Vogler, *Transition Metal and Rare Earth Compounds Excited States, Transitions, Interactions I*, ed. H. Yersin, Springer, New York, 2001.
41 T. Tröster, in *Handbook on the Physics and Chemistry of Rare Earths*, ed. K. A. Gschneidner, J.-C. G. Bünzli and V. K. Pecharsky, Elsevier, North-Holland, 2003, vol. 33, pp. 515–589.
42 M. D. Wisser, M. Chea, Y. Lin, D. M. Wu, W. L. Mao, A. Salleo and J. a Dionne, *Nano Lett.*, 2015, **15**, 1891–1897.

 

43 M. Runowski, in *Handbook of Nanomaterials in Analytical Chemistry*, ed. C. M. Hussain, Elsevier, 2020, pp. 227–273.
44 F. Datchi, A. Dewaele, P. Loubeyre, R. Letoullec, Y. Le Godec and B. Canny, *High Press. Res.*, 2007, **27**, 447–463.
45 R. G. Geitenbeek, H. W. De Wijn and A. Meijerink, *Phys. Rev. Appl.*, 2018, **10**, 1.
46 M. Suta and A. Meijerink, *Adv. Theory Simul.*, 2020, **3**, 2000176.
47 T. P. Swieten, D. Yu, T. Yu, S. J. W. Vonk, M. Suta, Q. Zhang, A. Meijerink and F. T. Rabouw, *Adv. Opt. Mater.*, 2021, **9**, 2001518.
48 J. D. Barnett, S. Block and G. J. Piermarini, *Rev. Sci. Instrum.*, 1973, **44**, 1–9.
49 S. Goderski, M. Runowski, P. Woźny, V. Lavín and S. Lis, *ACS Appl. Mater. Interfaces*, 2020, **12**, 40475–40485.
50 S. F. León-Luis, J. E. Muñoz-Santiuste, V. Lavín and U. R. Rodríguez-Mendoza, *Opt. Express*, 2012, **20**, 10393.
51 H. Arashi and M. Ishigame, *Jpn. J. Appl. Phys.*, 1982, **21**, 1647–1649.
52 G. Chen, J. Hölsä and J. R. Peterson, *J. Phys. Chem. Solids*, 1997, **58**, 2031–2037.
53 N. J. Hess and G. J. Exarhos, *High Press. Res.*, 1989, **2**, 57–64.
54 Y. R. Shen and W. B. Holzapfel, *Phys. Rev. B: Condens. Matter Mater. Phys.*, 1995, **51**, 15752–15762.
55 F. Datchi, R. LeToullec and P. Loubeyre, *J. Appl. Phys.*, 1997, **81**, 3333–3339.
56 M. Runowski, P. Woźny, V. Lavín and S. Lis, *Sens. Actuators, B*, 2018, **273**, 585–591.
57 J. Barzowska, T. Lesniewski, S. Mahlik, H. J. Seo and M. Grinberg, *Opt. Mater.*, 2018, **84**, 99–102.
58 C. Hernandez, S. K. Gupta, J. P. Zuniga, J. Vidal, R. Galvan, M. Martinez, H. Guzman, L. Chavez, Y. Mao and K. Lozano, *Sens. Actuators, A*, 2019, **298**, 111595.
59 M. Runowski, A. Shyichuk, A. Tymiński, T. Grzyb, V. Lavín and S. Lis, *ACS Appl. Mater. Interfaces*, 2018, **10**, 17269–17279.
60 M. Runowski, J. Marciniak, T. Grzyb, D. Przybylska, A. Shyichuk, B. Barszcz, A. Katrusiak and S. Lis, *Nanoscale*, 2017, **9**, 16030–16037.